STRUCTURING AND JOINING TRANSPARENT MATERIALS WITH ULTRA SHORT PULSE LASERS

Paper M601

Panjawat Kongsuwan, Sinisa Vukelic*, Y. Lawrence Yao

Columbia University, New York, NY, 10027, USA

Abstract

Nonlinear absorption of femtosecond-laser pulses enables the induction of structural changes in the interior of bulk transparent materials without affecting their surface. Features are generated by focusing the femtosecond laser pulses in the interior of a single glass piece to investigate change in morphology, mechanical properties, and ring structures of the modified region. Detailed characterization of the effect of laser irradiation is accomplished using differential interference contrast optical microscopy, spatially resolved Raman spectroscopy, and spatially resolved nanoindentation. A numerical model is also developed to predict an absorption volume inside transparent dielectric materials. After the better understanding of effects of optical and laser processing parameters on the resultant features is developed, the femtosecond laser pulses are finally focused on the interface of two glass specimens to implement transmission welding. The weld formation and geometry are discussed and indentation fracture analysis is used to investigate the strength of the weld seams.

Introduction

One of main advantages of femtosecond lasers in comparison to nanosecond ones is that they induce much less collateral damage due to heat conduction [1]. Furthermore, non-linear absorption, an unique property of femtosecond lasers, makes them particularly suitable for treatment of transparent dielectric materials [2]. Over the last decade, several research groups have studied the use of femtosecond lasers to process transparent materials. Davis et al. [3] and Glezer et al. [4] reported on the femtosecond laser induced changes in the interior of transparent materials, and discussed the potential for fabrication of photonic devices for telecommunication applications and three-dimensional optical data storages. These early reports prompted further investigation into the laser-matter interactions and the mechanisms for feature formation in transparent materials. When a femtosecond laser pulse is focused into the interior of the transparent dielectric materials, the laser intensity around the focal volume is extremely high and causes nonlinear absorption. Consequently, permanent structural modification occurs locally at the location of the laser focus. A study of the morphology of these structural changes showed that laser energy governs the size and the numerical aperture (NA) of the objective lens governs the shape of the affected region [5]. It was also shown that the features can be induced through mechanisms dominated by localized melting or explosive plasma expansion, depending on the laser and focusing parameters [6,7]. Bellouard et al. [8] studied fs-laser induced changes in morphology of fused silica through its effects on etching selectivity, increase of internal stresses and densification. Kucheyev and Demos [9] used photoluminescence (PL) and Raman spectroscopy to characterize defects created in the amorphous fused silica irradiated by nanosecond and femtosecond lasers with different wavelengths. Their PL results have shown that laser irradiation causes forming of non-bridging oxygen hole centers (NBOHC) and oxygen-deficiency centers (ODC). Raman spectroscopy revealed densification of the irradiated area. Chan et al. [10] used Raman scattering to investigate the effects of femtosecond laser irradiation on the interior of fused silica. They showed that ultrafast laser treatment causes a relative increase in intensity of the 495cm^{-1} and 606 cm^{-1} bands with respect to the main peak (440 cm^{-1}), and showed that this increase is a function of the incident laser energy. The area under the increased peak is qualitatively associated with densification of the material.

Laser assisted transmission welding using conventional nanoseconond (ns) lasers can be utilized when the top material is transparent to the laser and the bottom material is opaque to it [11]. The laser beam transmits through the top layer and is absorbed by the opaque material beneath. The subsequent heat accumulation helps to create the weld. When using an ultrafast laser, however, non-linear absorption enables structural changes in the interior of the target material without affecting the surface and thus the bottom material no longer needs to be opaque. Tamaki et al. [12] first demonstrated welding between two silica glass plates

* currently on faculty of Bucknell University

without a light-absorbent intermediate layer using a low repetition rate femtosecond laser. Watanabe et al. [13] subsequently reported the welding of dissimilar transparent materials using a femtosecond laser with similar characteristics. Further Watanabe et al. [13] investigated the parameters that resulted in joining of dissimilar samples by varying the laser pulse energy and the translation velocity. Tamaki et al. [14] conducted tensile tests to determine the joint strength; however, the testing procedure was not precise because of inability to continuously increase the applied load. Further studies [15–17] on the possibility of ultrashort pulsed laser welding of borosilicate glass substrates in the high repetition rate regime have been reported; however, there has been no quantitative evaluation of joint strength and no studies on the mechanical properties of the weld seam. There are many attempts to simplify the problem by characterizing mechanical properties of the molten region irradiated by an ultrashort pulse laser inside a single piece of transparent material. Miyamoto et al. [18] evaluated the mechanical strength of the laser-melt zone using a three-point bending test, and showed that the strength in that zone was as high as in the un-irradiated base material; however, the sample had to be polished to locate the laser induced feature on the bottom surface of the test sample in order to maximize the tensile strength. Borrelli et al. [19] performed a double torsion test to measure fracture toughness, and revealed that the apparent fracture toughness is increased within the laser-treated area. Bellouard et al. [20] used nanoindentation tests to show an increase in Young's modulus within the laser treated zones of fused silica irradiated by femtosecond pulses with high repetition rate; however, these measurements were not constrained to within the treated regions.

Studies referenced above address changes in properties and morphology which are a consequence of structural alterations due to the ultra-fast laser irradiation of the interior of transparent materials, explain the physical process that leads to those changes, and demonstrate the feasibility of transmission welding using femtosecond lasers. However, further investigation is still required. An important advancement in understanding of the changes in morphology, mechanical properties, and structure of glass subject to femtosecond laser irradiation is reviewed here. In order to simplify characterizations, experiments are conducted using single-piece specimens. Diffraction interference contrast (DIC) microscopy is employed to study morphology, a numerical model is developed to predict the feature shape, spatially resolved nanoindentation is used to investigate the change in mechanical properties. Spatially resolved confocal Raman spectroscopy is employed as a non-destructive characterization technique to examine structural changes of the fused silica glass within the affected region. The results have revealed local densification and relative volume fraction changes of the ring structures within the laser-irradiated and in the surrounding regions. Transmission welding using a femtosecond laser at a low repetition rate has been done to investigate the morphology and mechanical properties of the weld zone, and indentation fracture analysis is performed to study the fracture toughness and fracture strength of the material in the weld seams.

Femtosecond Laser Irradiation of Transparent Dielectric Materials

When femtosecond laser pulses are focused in the interior of a transparent material, the laser intensity within the focal volume becomes extremely high resulting in nonlinear absorption. When the laser intensity (photon flux) is above 10^{13} W/cm^2 [2] multiphoton ionization takes place as N photons of same wavelength λ with energy $h\nu$ simultaneously hit a bound electron. If the absorbed energy is greater than the atomic ionization potential ε the electron is freed from the valence. Free electrons produced by multiphoton ionization serve as seeds for subsequent avalanche ionization, through which a substantial number of free electrons will be produced. The probability of multiphoton ionization per atom per second, w_{mpi}, and that of avalanche ionization per unit time w_{avi}, are written as [21] :

$$w_{mpi} \approx \omega_{ph}^{3/2}\left(\frac{\varepsilon_{OSC}}{2E_I}\right)^{n_{ph}}; \qquad w_{avi} \approx \frac{\varepsilon_{OSC}}{E_I}\left(\frac{2\omega^2 v_{eff}}{\omega^2+v_{eff}^2}\right) \qquad (1)$$

where ω is the laser frequency, v_{eff} is the electron-phonon collision frequency, n_{ph} is the number of photons necessary for the electron to be transferred from the valence to the conduction band, E_I is the ionization energy, and ε_{OSC} is the electron quiver energy in the laser field. ε_{OSC} has units of eV and is expressed in a scaling form, $\varepsilon_{osc} = 9.3(1+\alpha^2)I\lambda^2/10^{14}$, where α is the coefficient for beam polarization, I is the laser intensity in units of W/cm^2, and λ is the laser wavelength in units of μm. The density of free electrons, n_e, from the two major mechanisms, multiphoton and avalanche ionization is [21] :

$$n_e(I,\lambda,t) = \left(n_0 + \frac{n_a w_{mpi}}{w_{avi}}[1-e^{-w_{avi}t}]\right)\times e^{w_{avi}t} \qquad (2)$$

where n_0 is the density of initial seed electrons, n_a is the density of neutral atoms, and t is time. When the free electron density reaches the critical value, n_{cr}, the

ionization threshold is achieved, and plasma is created in the material. This critical free electron density is described as [22]:

$$n_{cr} = \frac{\pi m_e c^2}{e^2 \lambda^2} = \frac{m_e \omega^2}{4\pi e^2} \quad (3)$$

where m_e is the electron mass, c is the speed of light, e is the electron charge, and λ is the laser wavelength. The free electron density is saturated in a few femtoseconds at the beginning of the laser pulse. During the remaining part of the pulse, plasma strongly absorbs the laser pulse energy, which creates a region of high energy density. Subsequently after the end of laser pulse, the transfer of the energy from the hot plasma to the lattice results in structural changes in the bulk transparent material [22].

Depending on the optical and laser processing parameters, the bulk transparent material can be modified through the micro-explosions or thermal accumulation mechanisms [23]. The micro-explosion occurs when a single laser pulse is deposited into the target material; high laser intensity is created either by tight focusing (NA > 1) of low energy laser pulse or relatively loose focusing (NA > 0.4) of high energy laser pulse resulting in a shock wave generation. The shock wave carries matter and energy away from the focal volume, compressing the surrounding material while a rarefaction wave behind the shock front propagates into the opposite direction, creating a rarified central region or void [24]. As a result a void surrounded by densified shell is generated. The thermal accumulation mechanism occurs, when multiple pulses either with low energy and high repetition rate or with high energy and low repetition rate are irradiated at same location or at low scanning speed. Due to short time between two consecutive pulses the heat produced by the single pulse does not have enough time to disperse into the surrounding material causing heat accumulation inside of the focal volume which effectively behaves as a point heat source. The localized melting of the material in the immediate vicinity of the heat source takes place and this is followed by heat conduction into the surrounding material. Due to rapid resolidification the melted region subsequently solidifies into a higher density phase [25]. In the latter mechanism, the feature size is determined by a combination of pulse energy and repetition rate, the stage translation speed, and the NA of the objective lens.

Experimental Setup and Characterization

Experiments have been conducted utilizing a chirped amplified Ti:Sapphire laser system which outputs high energy ultrashort pulses with 800 nm wavelength and 130 fs pulse duration at a 1 kHz repetition rate. The laser beam was focused by 40x objective lens with NA 0.60 into the interior of 1.0 or 1.6 mm thick S1-UV grade fused silica specimen and at the interface between 1.0 mm thick commercial grade borosilicate glass (BK7) plates. Samples were mounted on an Aerotech motorized linear stage. Different conditions of laser processing parameters were applied by varying the feed rate of the stage and the energy of the laser pulses.

After the femtosecond laser treatment, the samples were then sectioned, ground and polished with cerium-oxide and a leather polishing pad. Due to the transparency of the sample, transmitted-light differential interference contrast (DIC) optical microscopy was utilized to increase contrast and reveal the feature morphology. The affected region was examined via confocal micro-Raman spectroscopy to characterize structural changes. Nanoindentation was utilized to analyze mechanical properties of the laser treated region. For this purpose a three-sided Berkovich indenter tip was employed, which has advantage that the edges of the pyramid are more easily constructed to a sharper point than the four-sided Vickers geometry, and is generally used in small-scale indentation [26]. Shallow depth spatially resolved nanoindents with it correspondent minimum spacing in the x and z directions were conducted to cover both the affected and unaffected regions of the cross-section. High load nanoindents were also performed on the treated areas to induce cracks in order to investigate the fracture toughness and fracture strength.

Experimental Morphology by Transmission DIC

Morphology of the feature created via a single pulse with an energy of 30 μJ can be observed from the side view via DIC optical micrograph, shown in the Fig. 1.

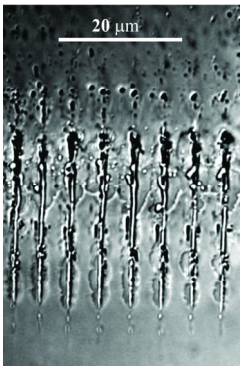

Figure 1: DIC optical microscope side-view (y-z plane) of features created via single femtosecond laser pulses in fused silica sample. Pulse energy is 30 μJ [23].

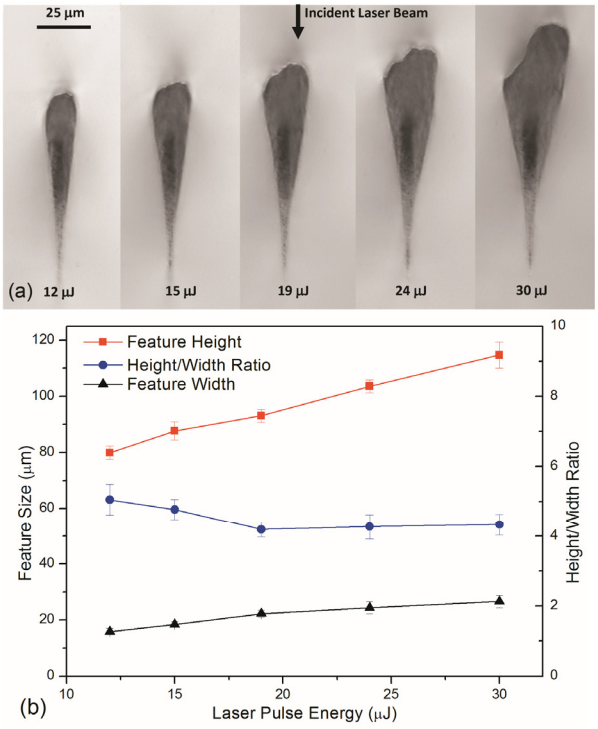

Figure 2: (a) Transmission DIC optical microscopy of cross section view (x-z plane) of femtosecond laser-irradiated fused silica (beam diameter of 1.5 µm, scanning speed of 0.04 mm/s, and repetition rate of 1 kHz) and (b) height, width, and height/width ratio of the features in Fig.2 (a) in femtosecond laser-irradiated fused silica at laser scanning speed of 0.04 mm/s. Error bars denote standard deviation [28].

The feature appears to be long and narrow with the very bright cylindrical region in the middle. High contrast between the inner region and the surrounding material suggests steep changes in refractive index which originates from differences in density. Thus it appears that high contrast features are actually voids, and the mechanism responsible for this feature generation is explosive plasma expansion. The cross sections of features created by different laser pulse energies with a scanning speed of 0.04 mm/s and by 30 µJ laser pulses at various feed rates are seen clearly with the use of DIC optical microscopy as shown in Fig. 2 (a) and Fig. 3 (a) respectively. These features have a long and narrow teardrop shape with an ellipsoidal dark core in the center. The distinctive color of this region could be a consequence of the high level of interaction of a material with laser pulses, which repeatedly deposits energy into this region with large overlap. The outer regions show some discoloration and are expected to have experienced a temperature equal or greater than the softening point of fused silica, and the mechanism responsible for this feature generation is thermal accumulation. The asymmetric shape of outer regions is considered to be the result of focusing effects [22] and different temporal slices of the energy above the threshold [5,16]. The irregular profile near the top area of the features is probably caused by the inhomogeneous distribution of the laser intensity rather than material properties. Due to the nature of the process, the focal volume can be seen as heat source. The inner region is darker and can be associated with focal volume where laser energy is directly deposited and the presence of the outer region is due to heat conduction between the focal volume and surrounding material [18,23,25]. From Fig.2 (a) and Fig. 3 (a), it can be seen that the feature size is strongly dependent on the scanning speed and laser pulse energy. The higher the laser pulse energies and lower feed rates correspond to formation of larger features. This is particularly important for transmission welding of the glasses in flat panel display industry where components inside of the enclosure can be thermally sensitive and highly localized weld is desired.

Figures 2 (b) and 3 (b) show the feature heights, widths, and aspect ratios (height/width) as a function of laser pulse energy and laser scanning speed respectively. The feature heights and widths are

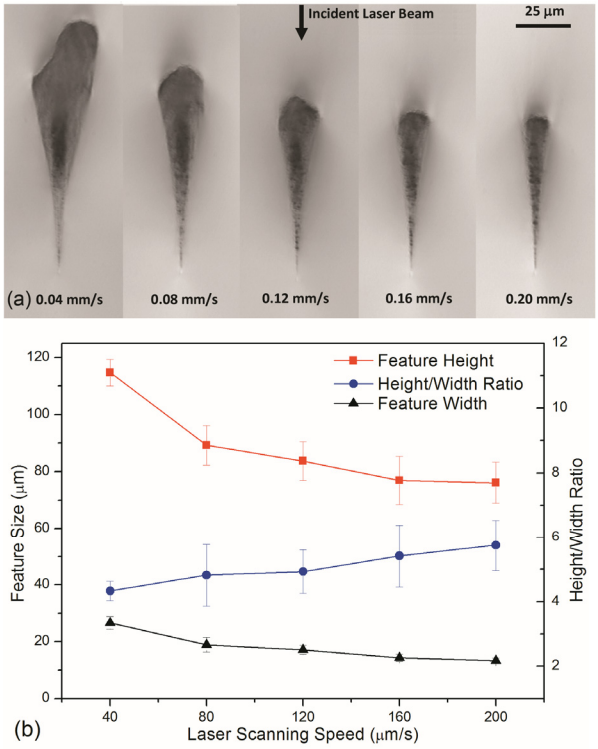

Figure 3: (a) Transmission DIC optical microscopy of cross section view (x-z plane) of femtosecond laser-irradiated fused silica (beam diameter of 1.5 µm, pulse energy of 30 µJ, and repetition rate of 1 kHz) and (b) height, width, and height/width ratio of the feature in Fig.3 (a) in femtosecond laser-irradiated fused silica at pulse energy level of 30 µJ. Error bars denote standard deviation [28].

respectively defined from the longest and the widest portions of both regular and irregular features. For higher laser pulse energies, the temperature in the focal volume is higher, and when it is conducted to the surrounding area, the affected region which experiences the temperature above the softening point is bigger in both directions as shown in Fig. 2 (b). On the other hand, the higher the speed, the less time there is for heat to accumulate inside the focal volume. As a result, the temperature is lower, and the affected region is smaller both in height and width as shown in Fig. 3 (b). At same laser scanning speed, 0.04 mm/s, the aspect ratios are more-or-less constant with the laser pulse energy in the range of this study as shown in Fig. 2 (b). This suggests that each area of the material is processed for the same amount of time and there is no change in the focal volume ratio, suggesting that the percentage of increase in size in each direction due to different pulse energies is about the same. However, from Fig. 3 (b) the aspect ratios are decreased when the laser scanning speed is decreased similarly as observed by Vukelic et. al. [23]. Since the temperature gradients between the focal volume and the surrounding material in the axial and lateral directions are different due to the Gaussian ellipsoidal shape of the focal volume, heat flux will be greater and conduction will be stronger in the lateral direction. Thus, the percentage of increase in size in this direction is higher than another direction as a function of time, resulting in the decreased aspect ratios.

Absorption Volume Modeling

To model the absorption volume shape, one should consider both temporal and spatial distribution characteristics of femtosecond laser pulses, and also account for the focusing characteristics of a collimated laser beam through transparent materials. In a transparent material, significant absorption is not achieved below a specific intensity threshold. This model aims to determine the locations within the material that achieve this intensity as a function of time within the laser pulse duration. Based on the fundamentals of laser beams and optics, in order to accurately capture the shape of the absorption volume, a numerical model should be constructed by considering the Gaussian temporal distribution of laser power, *P(t)*, within the laser pulse duration as given in Eq. (4) as well as the Gaussian spatial distribution of the laser intensity, *I(x,y,t)*, as given in Eq. (5).

$$P(t) = \frac{E_p\sqrt{4\ln 2}}{\sqrt{\pi}t_p}\exp[-4\ln 2(\frac{t-2t_p}{t_p})^2] \qquad (4)$$

$$I(x,y,t) = \frac{2P(t)}{\pi R_0^{\,2}}\exp[\frac{-2r^2}{R_0^{\,2}}] \qquad (5)$$

where E_p is the laser pulse energy, t_p is pulse duration, $r=\sqrt{x^2+y^2}$ is the distance from the center of laser beam, R_0 is the $1/e^2$ radius of the unfocused beam, and t is time. A laser beam with an intensity profile corresponding to Eq. (5) will converge to a diffraction-limited spot radius, w_o, and the beam waist as a function of distance from the focal plane, *w(z)*, can be calculated as

$$w(z) = w_0[1+(\frac{\theta z}{w_0})^2]^{1/2}; \qquad w_0 = \frac{M^2\lambda}{\pi NA} \qquad (6)$$

where z is the distance from the laser focal plane, Θ is the half-convergence angle of laser beam coming into the focus, M^2 is the laser quality factor, λ is the laser wavelength, and *NA* is the numerical aperture of an objective lens. At each point in time during the pulse duration, the spatial distribution of the laser intensity is described by Eq. (5). As the beam propagates into the sample, the width decreases as described by Eq. (6), and at some point, the laser intensity is absorbed at various locations forming a plasma when it reaches the intensity threshold, I_{th}, of the material given by [27]

$$I_{th} = (\frac{n_c}{n_a\tau_{rec}\beta_{mpi}})^{1/n_{ph}} \qquad (7)$$

where n_c is the electron critical density, n_a is the density of neutral atoms, β_{mpi} is the field ionization coefficient, and n_{ph} is the number of absorbed photons. The breakdown will start closest to the focal plane and move upwards along the beam axis during the first half of the pulse duration due to the Gaussian temporal distribution of the laser power. This requires a smaller beam spot to reach the threshold intensity at lower powers and a larger beam spot at higher powers. The absorption volume is determined by combining all of the points where absorption occurred during the first half of the laser pulse. The energy deposited in the second half of pulse will generate a high-density plasma in the absorption volume.

Figure 4 (a) shows the simulated cross sections of the absorption volume at different laser pulse energies. The cross section shape of the absorption volume indeed looks like the teardrop shape. The width and height of cross section increase with increasing laser pulse energy corresponding to experimental results reported in other studies [5,16,28]. Higher laser pulse energy leads to higher peak power, which generates higher local intensities at the same spot size.

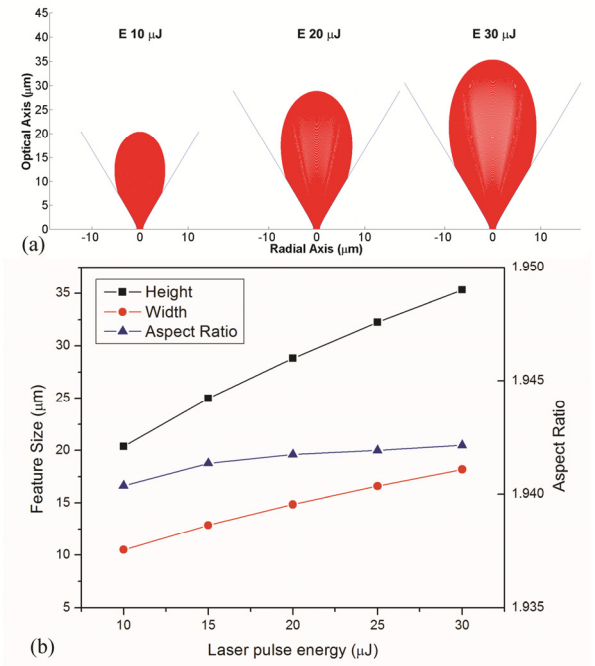

Figure 4: (a) Cross section view and (b) height, width, and height/width ratio of modeling absorption volume at different laser pulse energies (NA 0.6) [43].

Consequently, the material breakdown locations will be farther from the center in the radial axis, and will also be farther from the focal plane in the optical axis. Therefore, the height and width of the absorption volume for high laser pulse energies are greater than for low laser pulse energies as shown in Fig. 4(b). The aspect ratios of the absorption volumes at different laser pulse energies are more-or-less constant; a similar trend was observed for features created in single-piece specimen in a previous section. This trend agrees well with the focal volume aspect ratio calculated using the illumination point spread function, for which the ratio is constant and independent of laser pulse energy [29].

Figure 5 (a) shows the simulated cross sections of the absorption volume using different numerical aperture (NA) objective lenses for a fixed laser pulse energy. For high NAs, the teardrop shape of the absorption volume tends to have more-or-less equivalent size in height and width corresponding to the experimental results of Schaffer et al. [5]. Each point within the Gaussian intensity distribution of the unfocused laser beam requires a specific magnification to reach the intensity threshold of the material. This magnification defines the radius of the focused beam at which absorption will occur and is dependent of the NA of the objective lens. Therefore, the widths of absorption volumes are constant and independent of NA as shown in Fig. 5 (b). However, the corresponding breakdown locations of the material along the optical axis depend on the diffraction-limited spot size and the converging

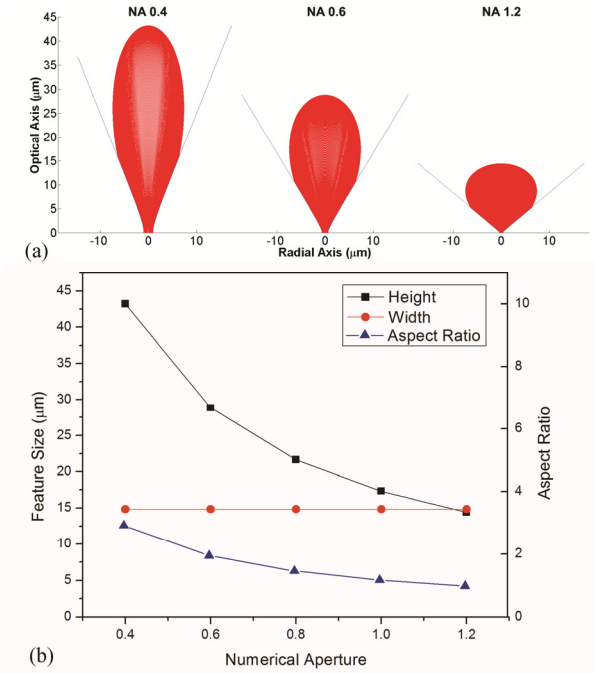

Figure 5: (a) Cross section view and (b) height, width, and height/width ratio of modeling absorption volume at different NAs (laser pulse energy of 20 μJ) [43].

angle of the focused laser beam. For higher NAs, the unfocused laser beam is converged at a greater rate; therefore the focused beam will achieve the required magnification and radius at a location closer to the focal plane along the optical axis. The heights of the absorption volumes are thus decreased with higher NAs as shown in Fig. 5(b). The aspect ratio of the absorption volume decreases with higher NAs, which corresponds well with the feature aspect ratio of the experimental results studied by Schaffer et al. [5].

Changes in Mechanical Properties by Nanoindentation

Nanoindentation or depth-sensing indentation testing is a modern technique which can be used to characterize the mechanical properties of materials at small length scales. An analysis of a load-displacement curve gives hardness and the elastic modulus of the indented material. An array of 200nm depth nanoindentation measurements were performed over the cross section of femtosecond laser-modified fused silica with spatial resolution of 5 μm as shown by the reflection DIC optical micrograph in Fig. 6. The load-displacement curves of indents on both modified and unmodified regions in Fig. 6 were measured, and the representative curves of these two regions were compared as illustrated in Fig. 7. Hardness and Young's modulus are extracted from the loading and unloading curves respectively.

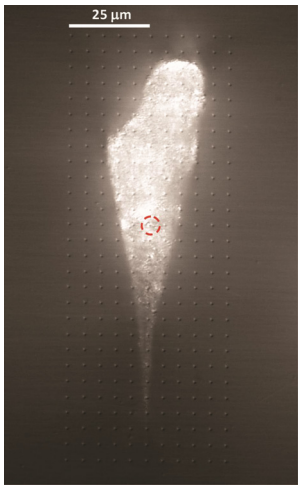

Figure 6: Representative reflection DIC optical microscopy of spatially resolved nanoindentation array (200 nm depth and 5 µm spacing) on the cross section (x-z plane) of fused silica irradiated by femtosecond laser (30 µJ pulse energy and 0.04 mm/s scanning speed). The circle locates the weakest point in Young's modulus and hardness corresponds to Fig.8 [28].

The contour maps of two basic material properties, Young's modulus and hardness, correspond to the array of nanoindents in the optical micrograph were plotted as shown in Fig. 8 (a) and (b). It is observed that the Young's modulus and hardness in the femtosecond laser-irradiated region are reduced, and that the size and shape of these contours look similar to the morphology of the affected region in Fig. 6. The reduction in modulus and hardness confirms presence of structural modifications inside the affected region. The region undergoes irreversible densification which is a consequence of high pressures created by the plasma expansion. At the same time the presence of breaks in the linkage within a structure due to the nature of the process also allows easier displacement of the atoms and reduces the elastic modulus [30].

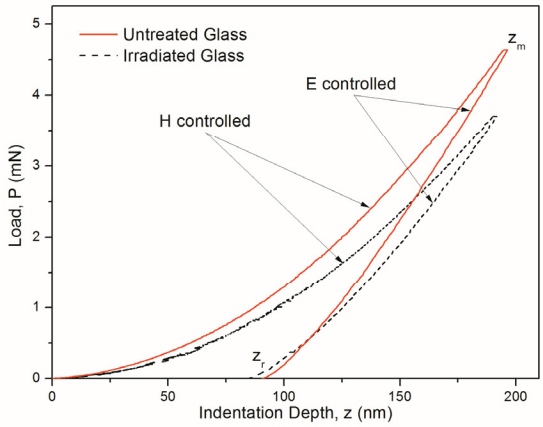

Figure 7: Representative load-displacement curves for 200 nm indentation in untreated and irradiated regions of fused silica sample [28].

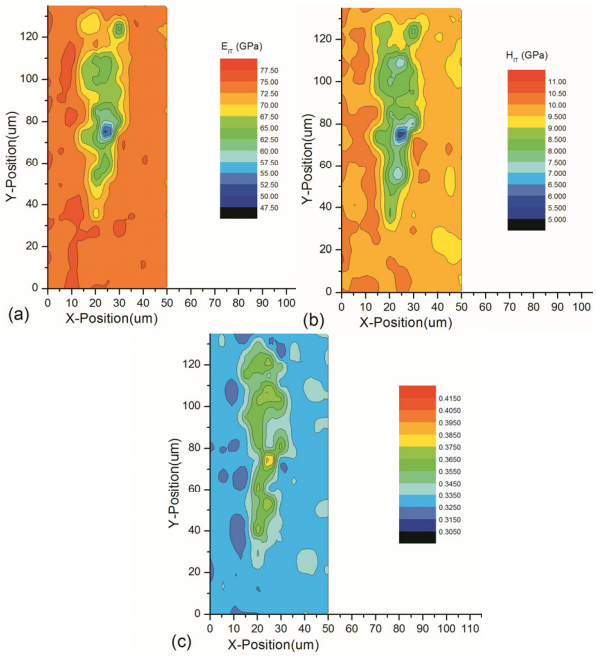

Figure 8: Spatially resolved determination of (a) Young's modulus, (b) hardness, and (c) normalized dissipated energy (ductility index) on the cross section of laser-irradiated region (30 µJ pulse energy and 0.04 mm/s scanning speed). The maps correspond to the array of 200 nm depth nanoindents with 5 µm spacing shown in Fig. 6 and are constructed based on the load-displacement measurement results shown in Fig. 7 [28].

Young's modulus should be proportional to the number of bridging bonds per unit volume of glass [31], and the hardness relates to the connectivity of the structure [32]. Fluorescence microscopy has shown that in fused silica nonbridging oxygen hole centers (NBOHC) are formed in the regions exposed to femtosecond laser irradiation especially in high pulse energy regime [33]. NBOHC are considered as defects, and cause the connectivity of glass network structure to be decreased. Therefore, the combination of high pressure and high temperature generated by femtosecond laser pulse trains cause the material in the affected region to become more flexible (lower E) and softer (lower H).

An energy-based analysis is another approach that is used to determine elastic recovery, densification energy [34], and ductility [35] from load versus displacement curves obtained through indentation testing. Ductility is typically defined as the degree of plastic strain at fracture. The ductility index, D, is defined in terms of the indentation energy ratio as the following [35].

$$D = \frac{U_r}{U_t} = \frac{U_t - U_e}{U_t} = 1 - \left(\int_{z_r}^{z_m} P_{ld}\,dz \Big/ \int_{0}^{z_m} P_{ud}\,dz \right) \qquad (8)$$

Where U_r is the irreversible hysteresis energy, U_t is the total applied energy, U_e is the elastically-recovered energy, z_r is the residual indentation depth, z_m is the maximum indentation depth, P_{ld} is the indentation load during loading, and P_{ud} is the indentation load during unloading. The ratio of the irreversible hysteresis loop energy U_r to the total energy U_t, is defined as the degree of plastic flow [35]. The ductility index D varies from 0.0 for a purely elastic to 1.0 for a purely plastic material. With the "open" network structure of fused silica, it is considered that the main mechanism for plastic deformation is densification rather than plastic flow [36], and that the irreversible hysteresis loop energy U_r can also be defined as the energy consumed for the densification [34]. A mapping of the results from this approach is illustrated in Fig. 8 (c). The contour map showed that ductility index of femtosecond laser-irradiated region is increased up to 25%.

Changes in Ring Structures and Their Volume Fractions by Raman Spectra

One of the main characteristics of amorphous solids is the lack of regularly repeating groups of atoms which are native to crystalline materials. Amorphous fused silica belongs to the group of so-called associated

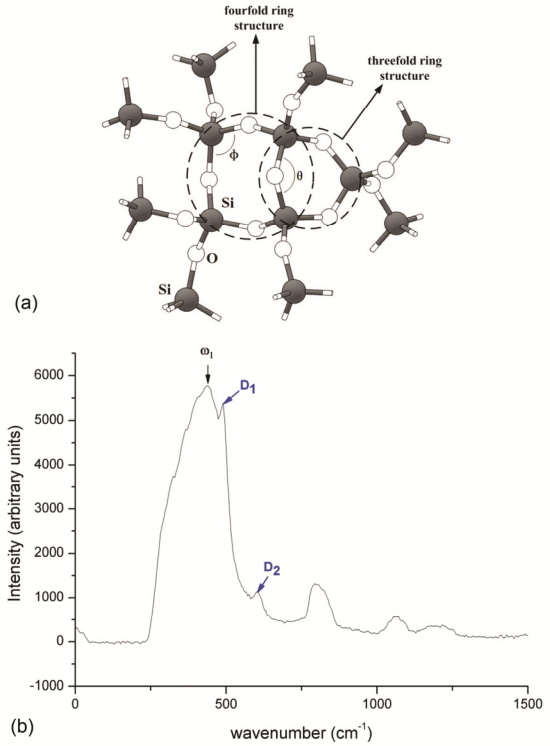

Figure 9: (a) Ball and stick model of the random network in the fused silica, showing three-fold and four-fold ring structures (encircled) and (b) typical Raman spectra of as received fused silica sample [39].

liquids [37] which form bonds in definite vectorial positions in space, leading to the formation of ring structures that connect molecules. In the case of amorphous solids, these rings then form a random network. A random network of atoms in fused silica is illustrated in Fig. 9 (a). In fused silica, most of the ring structures contain five or six ring members. This is due to the fact that the angle between O-Si-O bonds is approximately 133°, suggesting that larger ring structures are formed from almost perfect tetrahedrons which require minimal strain energy for their formation. In contrast, the formation of three and four member rings requires smaller O-Si-O angles (around 102° and 109°, respectively) [38] which has the consequence of distorting the tetrahedrons that create these ring structures. Thus, the strain energy required for the formation of these rings is higher than for the formation of $n \geq 5$ membered rings. Each of the n-fold ring structures present in the random network has a particular vibration frequency, or more precisely narrow band, due to the angle θ between tetrahedral components of the ring. Therefore, the main band in the Raman spectra of fused silica as shown in Fig. 3, denoted as ω_1 can be resolved into a peak located at 440 cm^{-1} which corresponds to the molecular vibration of the five and six-fold ring structures [37] and two subpeaks located at 495 cm^{-1} and 606 cm^{-1} and denoted as D_1 and D_2 in Fig. 9 (b). D_1 and D_2 peaks correspond to the molecular vibration of the four-fold (θ=109°) and three-fold (θ=102°) ring structures [38], respectively. Moreover, broadening of the band is associated with the presence of higher order rings [37].

Decomposition of the Raman spectra in the region between wavenumbers 300 cm^{-1} and 630 cm^{-1}, where three distinctive peaks corresponding to the different ring structures were observed, was performed through a curve fitting process [39]. It is assumed that within the volume of interest four different structures coexist three-, four-, five- and six- membered rings. The ratio between the integrated intensity of a particular n-fold ring and the total integrated intensity represented the percentage of that ring structure in the probed volume. Figure 10 (a), (b), and (c) depict cross section contour maps of the change in volume fraction of the five- and six-, four- and three-fold ring members for laser-irradiated region with pulse energy of 30 μJ and feedrates of 0.04 mm/s, respectively. From Fig. 10 (a), it can be seen that the content of higher membered rings decreases sharply from the untreated region towards the center of the focal volume where laser intensity is highest. Also it should be noted that two regions can be distinguished, an inner region where the content of the five- and six-fold ring members is lowest and constant and an outer region where it gradually increases to the equilibrium value. The inner

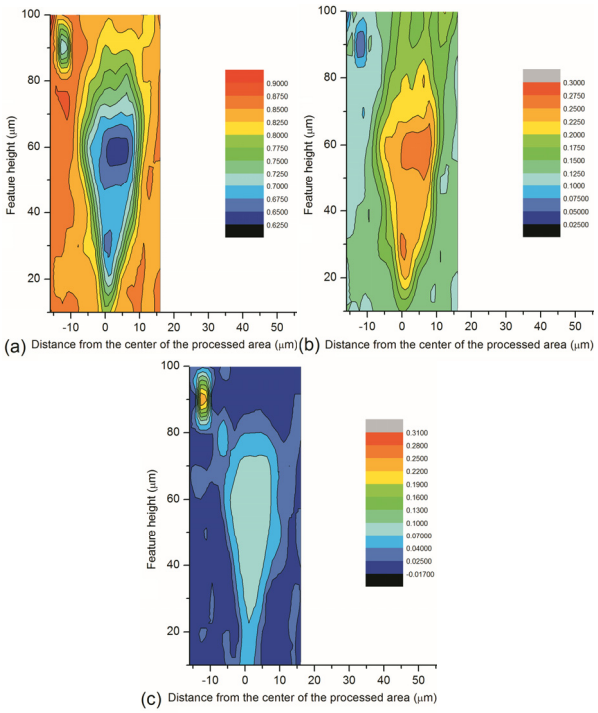

Figure 10: Volume fraction distribution of (a) five- and six-membered rings based on the 440 cm-1 peak, (b) four-membered rings based on the 495 cm-1 peak, and (c) three-membered rings based on the 606 cm-1 peak in Raman spectra of cross section of laser-irradiated region (pulse energy of 30 μJ and federates of 0.04 mm/s) [39].

region might be associated with the focal volume, where change is abrupt due to rapid solidification, leaving material frozen and the outer region would in that case be the surrounding affected region. On the other hand, the content of four-fold ring structures, associated with the 495 cm^{-1} peak, and that of three-fold ring structures, associated with the 606 cm^{-1} band increase from the untreated region towards the center of focal volume as seen in Fig. 10 (b) and (c). A similar trend to the one observed in Fig. 10 (a) is seen here. Two regions are formed: an inner region with a high and constant content of newly formed three- and four-fold rings and an outer one in which the amount of the rings decrease gradually with distance from the center. The change of random network structure from five- and six-fold rings to become three- and four-fold rings, which have smaller intertetrahedral angles and thus are more densely packed, suggested that fused silica irradiated by femtosecond laser pulses undergoes densification.

Weld Formation and Geometry

While other studies [17,18,40] have used high precision flatness glass plates and required the gap between the plates to be less than λ/4 in order that the welding to succeed, BK7 glass plates with standard

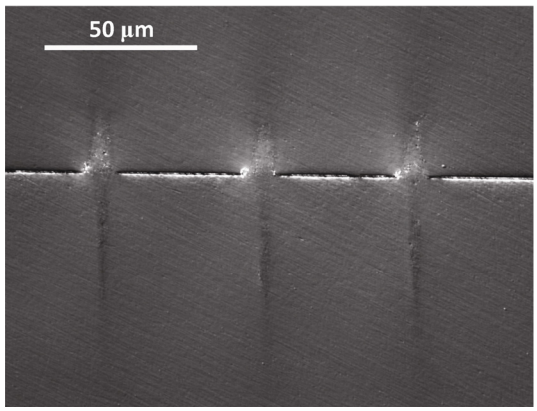

Figure 11: Reflective DIC optical microscopy of cross section view (xz-plane) of a weld seam (laser pulse energy of 10 μJ, scanning speed of 0.02 mm/s, and repetition rate of 1 kHz) [43].

flatness of 3-5 waves/inch were used in this study. Figure 11 shows the transmission welded cross section (xz-plane) of two BK7 glass plates with the processing condition of 10 μJ laser pulse energy and 0.02 mm/s laser scanning speed from reflective DIC optical microscopy. There is continuity of the material from the top piece to the bottom piece in the processed region. From this figure, it can also be observed that

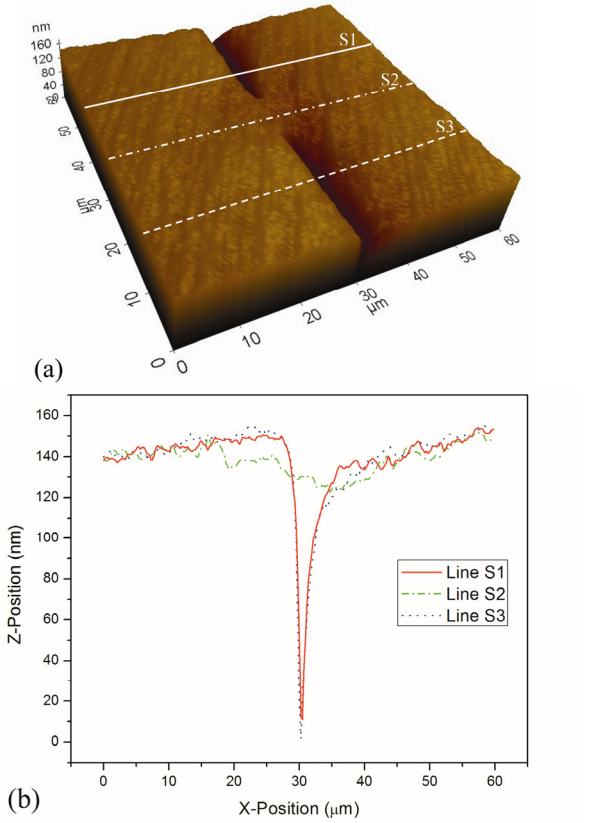

Figure 12: (a) 3D AFM topography on the cross section (xz-plane) of a weld seam (laser pulse energy of 10 μJ and scanning speed of 0.02 mm/s) and (b) AFM line profiles across glass interface near and on the weld seam [43].

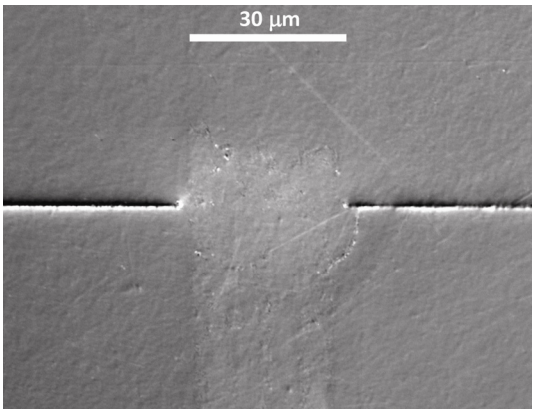

Figure 13: Reflective DIC optical microscopy of cross section view (xz-plane) of a multiple-line weld seam (laser pulse energy of 10 μJ, scanning speed of 0.02 mm/s, and repetition rate of 1 kHz, 5 scanning lines with 6 μm spacing between lines) [43].

the shape of the affected region is a teardrop shape and it looks similar to the morphology of femtosecond laser modified regions inside a single piece of a material. AFM topography was also carried out to image cross section profiles across both welded and reference regions as shown in Fig. 12 (a) and Fig. 12 (b). Although the gap between the plates is not as low as λ/4 due to the standard flatness of the plates, it is very clear that the two borosilicate glass plates were joined. In order to investigate the possibility of connecting multiple weld lines to have a larger weld seam, transmission welding of multiple laser scanning lines with the spacing between lines less than the weld width from the single line case was performed. Figure 13 shows the cross section view (xz-plane) of a sample processed with five overlapping weld lines. The individual weld lines cannot be distinguished, and it can be concluded that the transmission welding of large areas may be performed by automatically controlling the movement of a positioning stage and overlapping welds with a spacing less than the width of a single-line weld seam.

Fracture Toughness and Fracture Strength of the Weld Seam

The material in transmission welded region possesses properties different from that in the initial state. Nanoindentation is a non-destructive test capable of extracting elastic modulus and hardness of the specimen, and in addition to those properties, it is widely accepted that K_{IC} can also be obtained by measuring the post-indentation radial crack size emanating from the indent as a function of load [41].

$$K_C = k\left(\frac{E}{H}\right)^{1/2}\frac{P}{c^{3/2}} \tag{9}$$

where k is an empirical constant which depends on the geometry of the indenter, E and H is the indentation modulus and hardness, respectively, P is the indenter maximum load, and c is the crack length. For triangular pyramid indenters such as a Berkovich or cube corner, the profile of the radial crack is more likely a semi-elliptical geometry [42] rather than halfpenny shape observed for Vicker indenters. From the post-indentation radial crack, if the material is under a tensile load, fracture will occur when the stress intensity factor at the crack tip, K_I, reaches the critical stress intensity factor, K_{IC}, which is a physical characteristic of the material. The tensile fracture stress, σ_f, of the material corresponding to semi-elliptical surface cracks can be obtained as [43]

$$\sigma_f = \frac{K_{IC}\sqrt{\pi}\left[175/256 + 103r^2/256 - 27r^4/256 + 5r^6/256\right]}{2\sqrt{cr}[1 + 0.1215(1-r)]} \tag{10}$$

where K_{IC} is the fracture toughness from indentation, r is depth-to-length ratio of surface semi-elliptical cracks induced by a Berkovich indenter. Due to the presence of the crack, the residual strength of the structure decreases progressively with increasing crack size.

Fig. 14 shows a DIC optical image of cracks induced by a high load nanoindentation test. The bottom corner of the nanoindentation imprint is within the welded region, and the crack at the bottom corner extends across the weld at the interface between the two borosilicate glass plates. Comparing the crack lengths at the three corners of the nanoindentation imprint in Fig. 14, it is clear that the crack length in the welded region is shorter than those in unaffected region. Due to higher E/H ratio [43] and shorter crack length in the transmission welded region, it can be confirmed that the fracture toughness of material inside the welded region is increased which agrees with the fracture toughness increase observed in ultrafast laser-treated

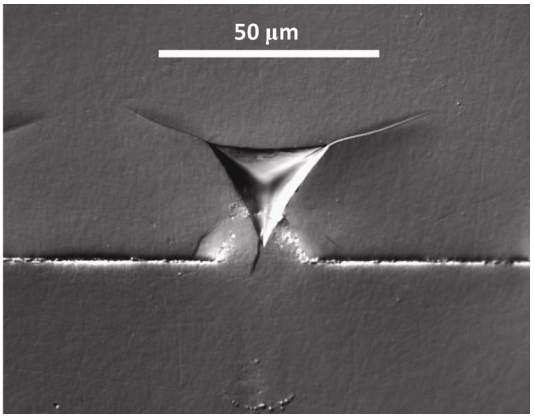

Figure 14: Reflective DIC optical microscopy of indentation fracture on cross section (xz-plane) of a weld seam (laser pulse energy of 30 μJ, scanning speed of 0.02 mm/s, and repetition rate of 1 kHz) [43].

areas of glasses obtained using double torsion tests by Borrelli et al. [19].

Figure 15 shows the indentation fracture toughness of material inside the weld seam compared to the reference material, and also shows the effect of laser pulse energy on the fracture toughness. In the ultrafast laser-treated region, there are more nonbridging oxygen hole centers (NBOHCs) [33] and the connectivity of the structure is decreased, and at the same time the remaining connected ring structures of material become more compact [39]. The presence of NBOHCs may help branch the main crack while a higher driving force is required to propagate the main crack through the more compact ring structure. Therefore, the fracture toughness of material in the weld seam is greater than in the reference material as shown in Fig. 15. The higher the laser pulse energy, the stronger the laser-matter interaction is inside the focal volume. It has been shown that there are more NBOHCs and more compact ring structures when processing is performed using higher pulse energies [33]. The presence of micro cracks are initially observed in the 30 uJ case and very distinctive in even higher laser pulse energy case [43]. Each of these micro cracks is a fracture surface which aids crack propagation, reducing the toughness of the material [44]. Therefore, there is an increasing trend in fracture toughness with pulse energy in the energy range of 10 – 25 μJ and the fracture toughness begins decreasing at a pulse energy of 30 μJ as shown in Fig. 15.

Figure 16 shows the tensile fracture stress of material in the reference and welded regions as a function of initial crack length. Due to the higher fracture strength at the same crack length, for a given crack size, the

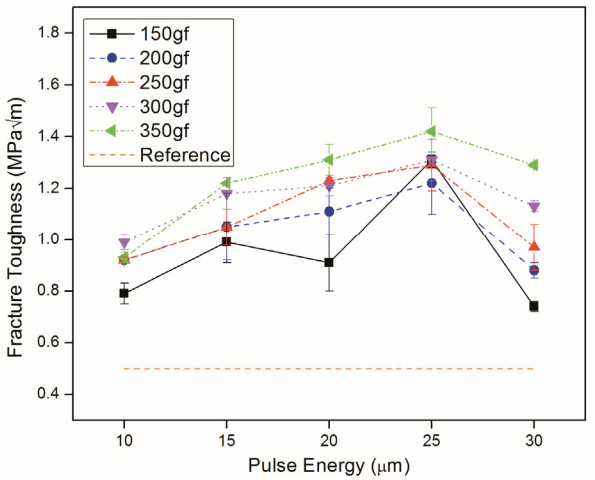

Figure 15: Fracture toughness of the material in welded regions with different laser pulse energy levels (10 μJ – 30 μJ) at fixed laser scanning speed of 0.02 mm/s and in a reference region from indentation fracture measurements at different loads. Error bars denote standard deviation [43].

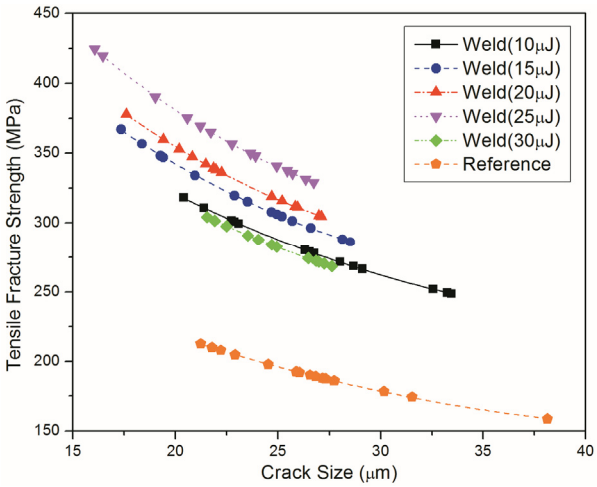

Figure 16: Fracture Strength as a function of crack size of the material in welded regions with different laser pulse energy levels (10 μJ – 30 μJ) at fixed laser scanning speed of 0.02 mm/s and in a reference region [43].

tensile stress required to fracture the weld seam is higher than the reference material. To obtain high fracture energy, it is necessary for glass to utilize energy absorbing processes [45]. It has been shown that several processes can toughen glass resulting in an energy absorbing process around the primary crack front and non-linear behavior prior to fracture [44]. The ultrafast laser-treated region, including the weld seam, could be analogous to a toughened processed zone; therefore, a higher stress is required to fracture the weld compared to the reference regions. This is consistent with concepts that suggest that toughening (increase K_{IC}) leads to strengthening (increase σf) especially for brittle solids such as glass [32]. The effect of the laser pulse energy on the fracture strength is also illustrated in Fig. 16. Due to the presence of micro cracks at sufficiently higher laser pulse energies as mentioned earlier in this section, it can be seen that the fracture strength does not monotonically increase with laser pulse energy, rather there is an optimum pulse energy beyond which the resultant fracture strength will decrease. However, the detrimental effect of the micro cracks is smaller than the beneficial effect of the compact ring structure (3-member rings) which has the highest barrier to fracture of all ring configurations [46]; therefore, the fracture strengths in welded regions for all laser pulse energy conditions in this study are still higher than the reference region.

Conclusions and Future Perspectives

It has been demonstrated that femtosecond laser irradiation is capable of modifying the morphology, mechanical properties, and ring structures of glass. The morphology of the structural alteration created via a single pulse as well as pulse trains with different laser

pulse energy and different feedrates has been investigated, and two different mechanisms (explosive plasma expansion and thermal accumulation) based on process conditions have been explored. A decrease in the Young's modulus and hardness were observed due to higher content of the NBOHC in treated regions that cause lower connectivity of the atomic structure caused by energetic pulse interaction with the material. However, the new structural material exhibits greater plastic behavior, and the ductility increases. A new quantitative method for analysis of the structural rearrangement of ring structures has been proposed. The method consists of spatially resolved identification of the volume fraction of ring structures within the probed volume through examination of Raman spectra. Upon irradiation with femtosecond lasers, the random network of fused silica reconfigures and the initially low presence of energetically unfavorable three- and four-membered rings increases at the expense of five- and six-membered rings, which leads to the densification of a modified area.

Transmission welding of two glass plates with standard flatness was successfully performed by using low repetition rate femtosecond laser irradiation. The weld morphology was investigated, and it was observed that the affected region is a teardrop shape similar to the features created by femtosecond laser irradiation of the interior of single piece transparent samples. A numerical model was developed to investigate the size and shape of the absorption volume as a function of laser pulse energy and numerical aperture of the objective lens. The model was able to predict the teardrop shape of the absorption volume, and the initial results suggest that higher laser pulse energies and higher numerical apertures are more desirable for transmission welding due to their wider weld widths and smaller affected regions. Large area transmission welding seams can also be formed by applying a multiple-line overlap welding process. The material inside the welded region revealed an increase in fracture toughness; therefore, a higher stress may be required to fracture the weld compared to the reference region. The geometry and mechanical properties of the weld seam obtained in this study suggest that transmission welding using low repetition rate femtosecond laser irradiation is a promising technique for spatially selective joining of glasses. In the future, it could be envisioned that with further investigation to improve the experimental controllability and reproducibility, to directly evaluate the joint strength, and to confirm impermeability, many applications can benefit from transmission welding of glass by femtosecond laser.

References

[1] Stuart B., Feit M., Rubenchik A., Shore B. & Perry M. (1995) Laser-Induced Damage in Dielectrics with Nanosecond to Subpicosecond Pulses, Physical Review Letters, 74(12), 2248-2251.

[2] Jiang L. & Tsai H. L. (2003) Femtosecond Lasers Ablation : Challenges and Opportunities, NSF Workshop on Unsolved Problems and Research Needs in Thermal Aspects of Material Removal Processes, Stillwater, OK, 1-15.

[3] Davis K. M., Miura K., Sugimoto N. & Hirao K. (1996) Writing waveguides in glass with a femtosecond laser, Optics letters, 21(21), 1729-31.

[4] Glezer E. N., Milosavljevic M., Huang L., Finlay R. J., Her T.-H., Callan J. P. & Mazur E. (1996) Three-dimensional optical storage inside transparent materials, Optics Letters, 21(24), 2023.

[5] Schaffer C. B., Jamison A. O. & Mazur E. (2004) Morphology of femtosecond laser-induced structural changes in bulk transparent materials, Applied Physics Letters, 84(9), 1441-1443.

[6] Schaffer C. B., Brodeur a, García J. F. & Mazur E. (2001) Micromachining bulk glass by use of femtosecond laser pulses with nanojoule energy, Optics letters, 26(2), 93-5.

[7] Glezer E. N. & Mazur E. (1997) Ultrafast-laser driven micro-explosions in transparent materials, Applied Physics Letters, 71(7), 882.

[8] Bellouard Y. (2006) Investigation of femtosecond laser irradiation on fused silica, Proceedings of SPIE, 6108, 61080M-61080M-9.

[9] Kucheyev S. O. & Demos S. G. (2003) Optical defects produced in fused silica during laser-induced breakdown, Applied Physics Letters, 82(19), 3230.

[10] Chan J. W., Huser T., Risbud S. & Krol D. M. (2001) Structural changes in fused silica after exposure to focused femtosecond laser pulses, Optics letters, 26(21), 1726-8.

[11] Tan a. W. Y. & Tay F. E. H. (2005) Localized laser assisted eutectic bonding of quartz and silicon by Nd:YAG pulsed-laser, Sensors and Actuators A: Physical, 120(2), 550-561.

[12] Tamaki T., Watanabe W., Nishii J. & Itoh K. (2005) Welding of Transparent Materials Using

Femtosecond Laser Pulses, Japanese Journal of Applied Physics, 44(No. 22), L687-L689.

[13] Watanabe W. (2006) Space-selective laser joining of dissimilar transparent materials using femtosecond laser pulses, Applied physics letters, 89(2), 21106.

[14] Tamaki T., Watanabe W. & Itoh K. (2006) Laser micro-welding of transparent materials by a localized heat accumulation effect using a femtosecond fiber laser at 1558 nm, Optics Express, 14(22), 10460.

[15] Bovatsek J., Arai A. & Schaffer C. B. (2006) Three-Dimensional Micromachining Inside Transparent Materials Using Femtosecond Laser Pulses : New Applications, CLEO/QELS and PhAST 2006, CA, 8-9.

[16] Miyamoto I. (2007) Fusion Welding of Glass Using Femtosecond Laser Pulses with High-repetition Rates, Journal of Laser Micro/Nanoengineering, 2(1), 57-63.

[17] Horn A., Mingareev I., Werth A., Kachel M. & Brenk U. (2008) Investigations on ultrafast welding of glass–glass and glass–silicon, Applied Physics A, 93(1), 171-175.

[18] Miyamoto I., Horn A., Gottmann J., Wortmann D., Mingareev I., Yoshino F., Schmidt M. & Bechtold P. (2008) Novel Fusion Welding Technology of Glass Using Ultrashort Pulse Lasers, Proc. 27th International Congress on Applications on Lasers & Electro-Optics, Temecula, CA, 112-121.

[19] Borrelli N., Helfinstine J., Price J. & Schroeder J. (2008) Glass Strengthening with an Ultrafast Laser, Proc. 27th International Congress on Applications on Lasers & Electro-Optics, Temecula, CA, 185-189.

[20] Bellouard Y., Colomb T., Depeursinge C., Dugan M., Said A. A. & Bado P. (2006) Nanoindentation and birefringence measurements on fused silica specimen exposed to low-energy femtosecond pulses., Optics express, 14(18), 8360-8366.

[21] Gamaly E. G., Rode a. V., Luther-Davies B. & Tikhonchuk V. T. (2002) Ablation of solids by femtosecond lasers: Ablation mechanism and ablation thresholds for metals and dielectrics, Physics of Plasmas, 9(3), 949.

[22] Gamaly E. G., Luther-Davies B., Hallo L., Nicolai P. & Tikhonchuk V. T. (2006) Laser-matter interaction in the bulk of a transparent solid: Confined microexplosion and void formation, Physical Review B, 73(21), 214101-1-15.

[23] Vukelić S., Kongsuwan P. & Yao Y. L. (2010) Ultrafast Laser Induced Structural Modification of Fused Silica—Part I: Feature Formation Mechanisms, Journal of Manufacturing Science and Engineering, 132(6), 061012.

[24] Juodkazis S., Misawa H., Hashimoto T., Gamaly E. G. & Luther-Davies B. (2006) Laser-induced microexplosion confined in a bulk of silica: Formation of nanovoids, Applied Physics Letters, 88(20), 201909.

[25] Schaffer C. B., García J. F. & Mazur E. (2003) Bulk heating of transparent materials using a high-repetition-rate femtosecond laser, Applied Physics A: Materials Science & Processing, 76(3), 351-354.

[26] Fischer-Cripps A. C. (2004) Nanoindentation, Springer, New York.

[27] Hallo L., Bourgeade A., Tikhonchuk V. T., Mezel C. & Breil J. (2007) Model and numerical simulations of the propagation and absorption of a short laser pulse in a transparent dielectric material: Blast-wave launch and cavity formation, Physical Review B, 76(2), 024101-1-12.

[28] Kongsuwan P., Wang H., Vukelic S. & Yao Y. L. (2010) Characterization of Morphology and Mechanical Properties of Glass Interior Irradiated by Femtosecond Laser, Journal of Manufacturing Science and Engineering, 132(4), 041009-1-10.

[29] Zipfel W. R., Williams R. M. & Webb W. W. (2003) Nonlinear magic: multiphoton microscopy in the biosciences, Nature biotechnology, 21(11), 1369-1377.

[30] Shelby J. E. (1997) Introduction to Glass Science and Technology, The Royal Society of Chemistry, Cambridge, UK.

[31] Charles R. (1961) A review of glass strength, Progress in ceramic science, 1, 1–38.

[32] Varshneya A. K. (1994) Fundamentals of Inorganic Glasses, Academic Press, Inc., San Diego, CA.

[33] Krol D. (2008) Femtosecond laser modification of glass, Journal of Non-Crystalline Solids, 354(2-9), 416-424.

[34] Suzuki K., Benino Y., Fujiwara T. & Komatsu T. (2002) Densification Energy during Nanoindentation of Silica Glass, Journal of the American ceramic society, 85, 3102-3104.

[35] Sakai M. (2011) The Meyer hardness: A measure for plasticity?, Journal of Materials Research, 14(09), 3630-3639.

[36] Hagan J. T. (1979) Cone cracks around Vickers indentations in fused silica glass, Journal of Materials Science, 14(2), 462-466.

[37] King S. V. (1967) Ring Configurations in a Random Network Model of Vitreous Silica, Nature, 213(5081), 1112-1113.

[38] Galeener F. (1979) Band limits and the vibrational spectra of tetrahedral glasses, Physical Review B, 19(8), 4292-4297.

[39] Vukelić S., Kongsuwan P., Ryu S. & Yao Y. L. (2010) Ultrafast Laser Induced Structural Modification of Fused Silica—Part II: Spatially Resolved and Decomposed Raman Spectral Analysis, Journal of Manufacturing Science and Engineering, 132(6), 061013.

[40] Miyamoto I. (2007) Local Melting of Glass Material and Its Application to Direct Fusion Welding by Ps-laser Pulses, Journal of Laser Micro/Nanoengineering, 2(1), 7-14.

[41] Lawn B. R. (1993) Fracture of Brittle Solids, Cambridge University Press, Cambridge, UK.

[42] Kese K. & Rowcliffe D. J. (2003) Nanoindentation Method for Measuring Residual Stress in Brittle Materials, Journal of the American Ceramic Society, 86(5), 811-816.

[43] Kongsuwan P., Satoh G. & Yao Y. L. (2012) Transmission Welding of Glass by Femtosecond Laser: Mechanism and Fracture Strength, Journal of Manufacturing Science and Engineering, 134(1), 011004.

[44] Mecholsky J. J. (1983) Toughening in Glass Ceramics, Fracture Mechanics of Ceramics, Volume 6: Measurements, Transformations, and High-Temperature Fracture, R.C. Bradt, A.G. Evans, D.P.H. Hasselman, and F.F. Lange, eds., Plenum Press, New York.

[45] Soga N. (1985) Elastic moduli and fracture toughness of glass, Journal of Non-Crystalline Solids, 73(1-3), 305-313.

[46] West J. (1999) The application of fractal and quantum geometry to brittle fracture, Journal of Non-Crystalline Solids, 260(1-2), 99-108.

Meet the Authors

Panjawat Kongsuwan received his M.S. from Columbia University. He is currently a doctoral student at the Manufacturing Research Laboratory at Columbia University.

Dr. Sinisa Vukelic received his Ph.D from Columbia University in 2009. He is currently on faculty of Bucknell University.

Dr. Y. Lawrence Yao is currently a professor of Columbia University's Mechanical Engineering Department and director of the Manufacturing Research Laboratory. He received his Ph.D from the University of Wisconsin-Madison in 1988.